

PAPER



Cite this: *J. Mater. Chem. C*,
2026, 14, 336

Received 20th August 2025,
Accepted 5th November 2025

DOI: 10.1039/d5tc03144c

rsc.li/materials-c

Mie-resonant silicon waveguide for efficient coupling with excitonic emitters in InSe

Maxim Rakhlin,^a Timofey V. Antipov,^b Alexandra D. Gartman,^{bc} Dmitry N. Gulkin,^b Lyubov Kotova,^a Aidar Galimov,^a Bogdan Borodin,^a Ilya Eliseyev,^a Alexander S. Shorokhov^b and Andrey A. Fedyanin^{*ab}

Enhancement of radiative coupling efficiency between out-of-plane excitonic emitters in an indium selenide (InSe) film and an integrated waveguide formed by silicon (Si) Mie-resonant nanodisks is experimentally studied. Photoluminescence power at the resonant waveguide output is increased by 2.5 times at 950 nm in comparison with the case of a conventional rib waveguide of the same geometrical parameters due to the efficient excitation of Mie-type magnetic dipole resonances in individual nanoparticles. These results show inspiring possibilities for creating new on-chip light emitters for various integrated photonics applications.

1. Introduction

Modern photonic technologies can offer various advantages over purely electronic ones, including faster signal processing and low energy consumption based on specially designed micro- and nanoscale devices. Optical chips for various applications such as LiDARs,¹ biosensors² and optical computers that transmit and process information using photons are under development.³ The main components of such devices, regardless of the specific task being solved, are light sources and waveguides that transmit and redirect optical radiation.⁴ Silicon is one of the most commonly used semiconductors in nanophotonics technology for waveguides, with a transmission region corresponding to the infrared region of the spectrum.^{5,6} However, silicon is not suitable for direct light generation, therefore efficient Si waveguide-compatible emitters operating effectively at these wavelengths are needed. It defines interest of the integrated photonics community to development of a new generation of light sources on a chip compatible with modern semiconductor technologies for increasing photo- and electroluminescence based on various emitter mechanisms such as Er-related light sources, Ge-on-Si lasers, III-V-based Si lasers and *etc.*⁷

Special attention is paid to excitonic light sources.⁸ They offer several advantages, including strong light-matter interaction, unique optical properties, wide spectral range, the potential for quantum devices and all-optical transistors.⁹ They are highly efficient, versatile, and enable precise control of light

emission properties.¹⁰ Excitonic devices hold potential for quantum computation, while all-optical transistors offer new possibilities for signal processing.¹¹ One of the most promising sources of excitonic luminescence with high-efficient coupling to waveguides are 2D materials, due to their large exciton binding energy, which can reach hundreds of meV.¹² 2D materials can be easily integrated into other systems or devices,^{13,14} as well as assembled into heterostructures with the desired functionality.^{15,16}

Transition metal dichalcogenides (TMDs) are widely known 2D materials as perfect sources of excitonic photoluminescence.^{12,17–20} The dipole moment orientation of excitonic emitters determines their coupling to waveguides. In case of TMDs, dipole moments of bright excitons are randomly oriented in-plane that lowers the efficiency of their radiation coupling to waveguides.²¹ Contrary, gray excitons, found in thin films of layered III–VI monochalcogenides like InSe, can be potentially suitable to solve this problem.^{22–24} These excitons allow the electron and hole to be separated into different layers, creating a dipole with an out-of-plane orientation.²⁵

InSe offers the large band-gap tunability: its optical band gap blue-shifts as the number of layers decrease.²⁶ InSe has weak electron-phonon scattering²⁷ and a low effective mass,^{28,29} resulting in high carriers mobility. The absence of inversion symmetry in certain polytypes of InSe crystals enables second-harmonic generation for all layer thicknesses.³⁰ These properties make InSe a great choice for various photonic and optoelectronic applications.^{31–33}

Efficient delivery of radiation from the emitter directly to the integrated circuit requires strong optical coupling between the emitter and the on-chip waveguide system. Such on-chip systems can be a compound of a large number of subwavelength particles supporting excitation of optical resonances. All-dielectric nanoparticles made of transparent materials with

^a Ioffe Institute, St. Petersburg, 194021, Russia

^b Faculty of Physics, Lomonosov Moscow State University, Moscow 119991, Russia.
E-mail: fedyanin@nanolab.phys.msu.ru

^c Department of Materials Science, Shenzhen MSU-BIT University, Shenzhen 517182, P.R. China

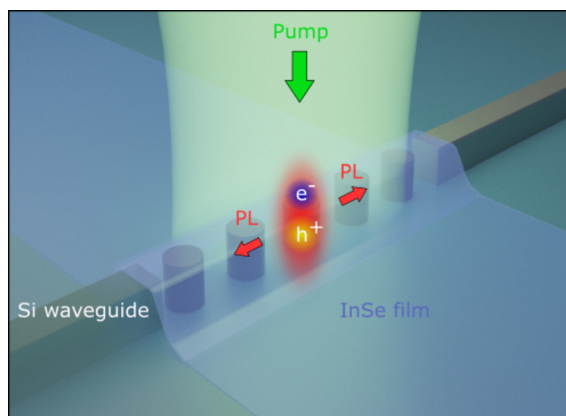


Fig. 1 The sketch showing optical coupling between the resonant silicon waveguide structure and the excitonic source localized in the InSe film.

a high refractive index are becoming increasingly popular alternatives to metal-based ones for light control in an integrated circuit.^{34–38} These particles support excitation of both electric (ED) and magnetic (MD) dipole Mie resonances and are compatible with modern complementary metal-oxide-semiconductor technologies (CMOS). By arranging such nanoantennas into one-dimensional chains and exciting the MD resonance in each particle, it is possible to achieve efficient propagation of radiation along the chain due to near-field optical coupling between neighboring particles.³⁹ It has been shown numerically, that placing InSe thin films and TMD heterostructures on such chains leads to increased optical coupling with the waveguide.^{40,41}

In this study, we experimentally demonstrate efficient coupling between integrated resonant waveguide structure based on Mie-type nanoparticles and thin films of InSe. To this end we fabricate silicon waveguides with embedded Mie nanoantennas and InSe flakes of specific thicknesses placed on the waveguides (see SI, Section S1 for the fabrication details). They support MD excitation which is field-complementary with excitonic emitters localized on defects in the InSe film covering the waveguide (Fig. 1). Micro-photoluminescence (μ -PL) experiments demonstrate an increase in emission intensity due to the enhancement of the optical coupling of the emitted light with the waveguide structure on the chip and due to the Purcell effect associated with the local field resonant enhancement. We support our experimental findings with numerical simulations that show the efficient coupling between out-of-plane excitons and integrated waveguides composed of resonant Si nanoparticles.

2. Sample under study

A typical array of silicon resonant nanoparticles waveguide (RW) made of a SOI-based wafer with a $2\ \mu\text{m}$ -thick oxide layer and $220\ \text{nm}$ -thick Si layer is shown in Fig. 2(a–d). The sample consists of several parts: a central part in the form of silicon nanodisks shaped as truncated cones and two $140 \pm 5\ \text{nm}$ -wide strips with the grating couplers at the edges (Fig. 2(a and b)). The distance between the disks is $50 \pm 5\ \text{nm}$, the diameter of the disks is $220 \pm 10\ \text{nm}$ and the height of the disks is

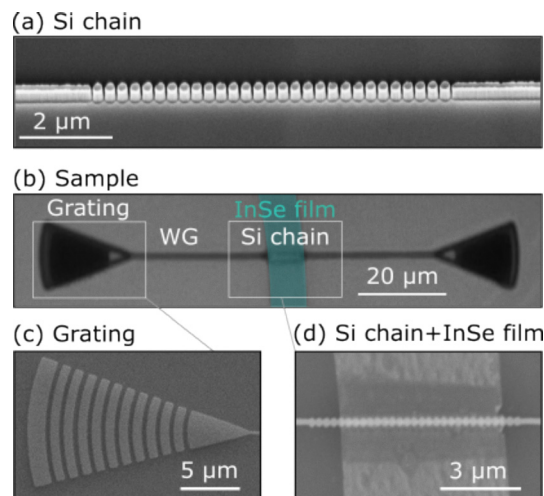


Fig. 2 (a) Scanning electron microscope (SEM) image of the chain before the film transfer. (b) Optical microscope image of the sample. (c) SEM image of the grating at the end of the waveguide. (d) SEM image of the chain combined with the InSe film.

$170 \pm 5\ \text{nm}$. Inter-disk spacing of $50\ \text{nm}$ is chosen based on fabrication constraints, specifically the resolution limits of lithography and etching. Increasing the inter-disk spacing significantly reduces the near-field coupling between disks, thereby degrading the overall transmission through the waveguide (see SI, Section S7). Nanoparticle parameters are selected to increase the efficiency of optical coupling between dipole emitters in InSe film and resonant waveguides due to the excitation of Mie-type resonances in the disks.⁴⁰ More specifically, the geometric parameters are selected to resonantly excite modes within the spectral range corresponding to the InSe film's emission wavelength (approximately $950\text{--}960\ \text{nm}$). To achieve this, we conducted numerical simulations of a single nanodisk under plane wave excitation with polarization perpendicular to the sample plane, as well as simulations of a nanodisk within the chain excited by a TM mode source through the waveguide input port. The results, presented in SI Section S8, reveal enhanced scattering within the target spectral region, confirming that the chosen disk dimensions optimize coupling efficiency by aligning the resonant scattering with the InSe emission spectrum. There are two focusing grating couplers at the ends of the waveguides, which are used to direct light out of the chip for measuring the fraction of radiation coupled to and transmitted through the waveguide (Fig. 2(c)). A silicon slab with a thickness of $50 \pm 5\ \text{nm}$ is also formed between the substrate and the waveguide system, and the total height of the structure is $220 \pm 10\ \text{nm}$. Numerical modelling of the system using the finite-difference time-domain (FDTD) method shows that this feature of the manufactured sample does not have any significant effect on the optical properties of the system under study. For the μ -PL measurements, a reference array of conventional rib waveguides (CW) without chain of nanodisks is also fabricated.

Further, the InSe flake obtained by employing the mechanical exfoliation technique is transferred onto the central part of the waveguide. Fig. 2(b, c and d) show the combination of the

film and RW in the experimental sample. The average film thickness measured by atomic force microscopy is 15 ± 5 nm. This value is optimal because, on the one hand, reducing the thickness of the film would lead to a blueshift in the photoluminescence spectrum⁴² and, on the other hand, increasing the thickness can negatively affect the transmission of the hybrid waveguide. Additional modeling (see SI, Section S10) demonstrates that for film thicknesses below approximately 40 nm, the coupling efficiency remains largely unchanged. However, for thicker films, the spectral overlap between the nanodisks' resonance and the film's emission spectrum decreases, leading to a reduction in the coupling efficiency.

3. Optical spectroscopy measurements

We perform the optical spectroscopy to characterize the resonant waveguide systems fabricated in our experiments. In these measurements, we use a home-built setup, the detailed representation of which is shown in SI, Section S3.

A schematic illustration of the experimental configuration in reflection scheme is shown by the inset image in Fig. 3. It enables simultaneous visualization of the entire sample, as well as the focusing of laser light on the input grating. Moreover, it allows the radiation transmitted by the output grating to be collected and spatially filtered. The TM-polarization of the laser beam is selected by the Glan-Taylor prism. The measured transmission spectrum of the RW is further normalized to the same spectrum obtained for the CW.

The experimental dependence of the relative transmission on the wavelength is shown in Fig. 3 by the red curve. The maximum at 915 nm corresponds to the most efficient optical coupling between the nanoparticles of the chain due to which

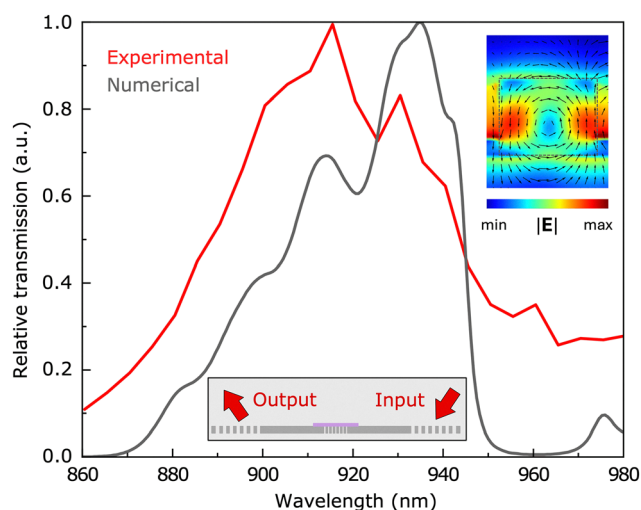


Fig. 3 Relative transmission spectra of the waveguides. Inset at the bottom shows a schematic illustration of the experimental configuration. Inset to the right shows the electric field distribution in the central disk cross-section at 937 nm.

the radiation propagates along it with the least losses. The relative transmission of the system is numerically calculated using FDTD method. For modeling, we use a Si waveguide 170 nm-high and 140 nm-wide with a central part in the form of a chain of 29 silicon nanodisks with a height of 170 nm and a spacing of 50 nm, covered with a 15 nm-thick InSe film. The disk diameters are set to a uniform distribution in the range 220 ± 10 nm in order to take into account fabrication imperfections. As in the experiment, a 50 nm-thick slab is placed between the sample and the oxide layer.

The source of the fundamental TM-mode is placed before the chain of nanodisks, and a power monitor, which is used to measure the transmission, after the chain. A similar simulation is carried out for the rib waveguide of the same length. In the simulations we use the perfectly matched layer boundary conditions. Dividing the spectrum for the nanoparticles chain by the spectrum of the conventional waveguide gives the relative transmission (gray curve in Fig. 3). The blueshift of the experimental spectrum can be explained by the imperfection of the fabricated structure. To elucidate the origin of the resonant feature observed in the transmission spectrum of the nanodisk waveguide, we conducted a multipole decomposition of the excited electric currents into Mie modes (see SI, Section S8). The analysis revealed that the magnetic quadrupole contribution dominates the total scattering cross-section, followed by significant contributions from the electric dipole and magnetic dipole modes. Additionally, we performed conceptual simulations to compare the coupling efficiencies of different Mie modes in the nanodisks with out-of-plane dipole emitters in the InSe film. Further details are provided in SI, Section S9.

4. Micro-Raman measurements

Raman spectroscopy is employed for structural characterization of the samples. Typical Raman spectrum of the InSe flake (Fig. 4(b)) consists of modes characteristic for β -InSe polytype⁴³: $E_g(1)$ (41 cm^{-1}), A_{1g}^1 (115 cm^{-1}), E_g^2 (178 cm^{-1}), E_u^1 (186 cm^{-1}), A_{1g}^2 (227 cm^{-1}) and a weak contribution of A_{2u} phonons (198 cm^{-1}).⁴⁴ In addition to point measurements, the samples are investigated by Raman mapping. Fig. 4(c) represents the intensity distribution of the A_{1g}^1 peak. Some enhancement (2–3x) of the Raman signal observing in the flake region above the resonator may be caused by the interference enhancement of the Raman signal by the resonator. The effect is similar to that was observed in thin flakes and films deposited on SiO_2/Si substrates.⁴⁵ The Raman map of the A_{1g}^1 peak position (Fig. 4(d)) reveals that its frequency varied by no more than 0.6 cm^{-1} , which is within the spectrometer resolution. According to the data obtained for a 10–15 nm-thick flake,⁴⁶ the strain shift rate of the A_{1g} Raman line is $-2.5 \text{ cm}^{-1}/\%$, thus, the variation of strain within the flake is significantly less than 0.24%. This indicates that, although placing the flake onto a waveguide is expected to cause strain in the InSe flake, the properties of InSe in the vicinity of the resonator are close to the properties of an unstrained InSe flake.

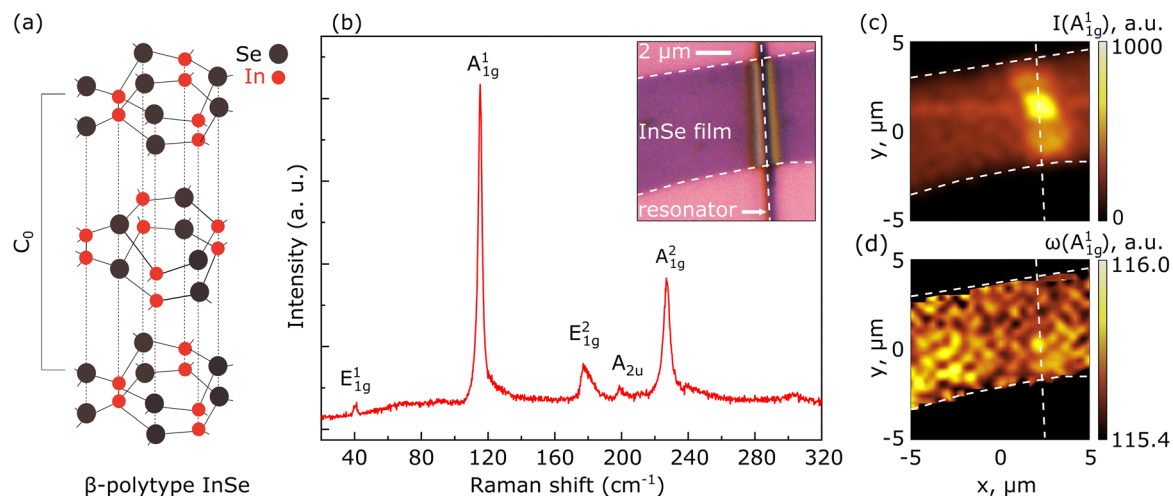


Fig. 4 Raman scattering studies: (a) Unit cell of β -InSe. (b) Typical Raman spectrum of the InSe flake under study. Inset shows an optical image of the area of by Raman mapping. (c) and (d) Raman scattering maps demonstrating the peak intensity and frequency distribution of the A_{1g}^1 Raman line in the vicinity of the waveguide. Dashed curves are the borders of the flake and the waveguide.

5. Micro-photoluminescence measurements

The μ -PL measurements of the sample are carried out at $T = 8$ K using the setup shown in SI, Section S4. The sketches at the top of the Fig. 5(a and b) illustrate the measurement concepts and the graphs below show the experimental results. The left figure corresponds to the excitation of the film located directly on the RW (red curve) and on the substrate without the structure (gray curve) and the collection of PL radiation emitted in back-scattering, while the right figure corresponds to the collection of PL through a grating coupler (radiation from the film in this case is blocked by a diaphragm) of the RW (red curve) and the CW (gray curve). From the Fig. 5(a), one can significant PL enhancement for the InSe film located on top of the resonant

nanodisks. These results are in line with other recent reports where all-dielectric resonant nanostructures were employed to boost light-matter interaction in 2D semiconductors.^{47,48} From the Fig. 5(b), one can also compare radiation coupling efficiency for the RW and CW. To do this, we divide the PL power of the RW at a wavelength of 950 nm by the corresponding value for CW. As a result, we get a 2.5-fold increase in the radiation coupling efficiency.

The main factors of PL power enhancement in the experiments are:

1. Local pump field enhancement due to the resonant nanophotonic structure under the InSe film leading to the increased absorption of the pump radiation.⁴⁰
2. Increase in the rate of spontaneous PL emission due to the Purcell effect.⁴⁹

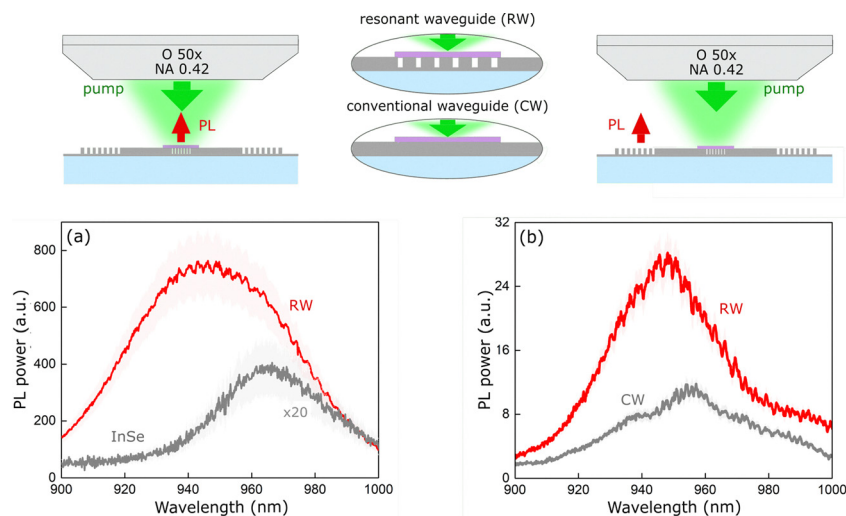


Fig. 5 μ -PL measurement results. The sketches above the graphs show the concept of measurements in the corresponding cases. (a) Spectra of μ -PL emitted in backscattering (red curve corresponds to the RW and gray curve corresponds to the InSe flake on the substrate). (b) Spectra of μ -PL extracted through the grating coupler (red curve corresponds to the RW and gray curve corresponds to the CW).

3. Increase in the number of emitters due to local strain in the film.^{21,50}

4. Optical radiation redirection effect: antennas not only inject radiation into the waveguide, but also re-scatter it into the objective lens.

We perform numerical modeling to quantify the individual contributions of different mechanisms to the total PL enhancement. Detailed simulation parameters and results are provided in the SI, Section S6 “Different mechanisms contributing to PL power enhancement.” Specifically, we demonstrate a 1.5-fold increase in pump absorption for the InSe film positioned on the nanodisks compared to the substrate, nearly a 2.5-fold enhancement of the Purcell factor, and an approximately 11-fold increase in emission directivity for the experimental configuration, where the back-scattered PL signal is detected from the same region on the film as the excitation spot.

We also calculate the fraction of radiation coupled into the waveguide:

$$\frac{2P_{\text{grat}}}{2P_{\text{grat}} + P_{\text{back}} + P_{\text{loss}}} \times 100\%,$$

where P_{grat} is the power on one grating (known from the Fig. 5(b)), P_{back} is the power in the back reflection (known from the Fig. 5(a)) and P_{loss} is the loss power (power of radiation absorbed in the waveguide). The last parameter is estimated from the calculated transmission of the waveguide (see SI, Section S5). According to the Fig. 5, the final result for the efficiency of the radiation coupling into the waveguide is 33% for the RW and 13% for the CW.

6. Contributions from variously oriented dipole emitters in InSe

The investigated nanoparticle waveguide is initially designed to couple efficiently with the out-of-plane dipole sources representing gray excitons in the InSe film placed on top of the structure. We perform additional modeling to clarify the dominant role of these emitters in the total PL radiation coupled into the waveguide. For this purpose, we consider variously oriented dipole emitters in the InSe film and numerically estimate for them the Purcell factor and radiation coupling efficiency (amount of the radiation power transmitted through the waveguide, normalized to the emitter power). In each simulation an electric dipole of the same power is placed above the central disk of the waveguide system: in its center and on its edge (which are considered to be two most probable positions due to the film strain). Three types of dipole orientation relative to the waveguide system are schematically shown at the top of the Fig. 6: out-of-plane (marked with the blue color), in-plane along the waveguide (marked with the red color), and in-plane across the waveguide (marked with the violet color). The bottom part of Fig. 6 shows the comparative pie-charts for these three dipole configurations, both for the resonant waveguide composed of nanodisks and the conventional rib waveguide. Different colors in these pie-charts correspond to the same colors used for marking different dipole orientations in the upper schematics. All contributions are normalized to the sum value,

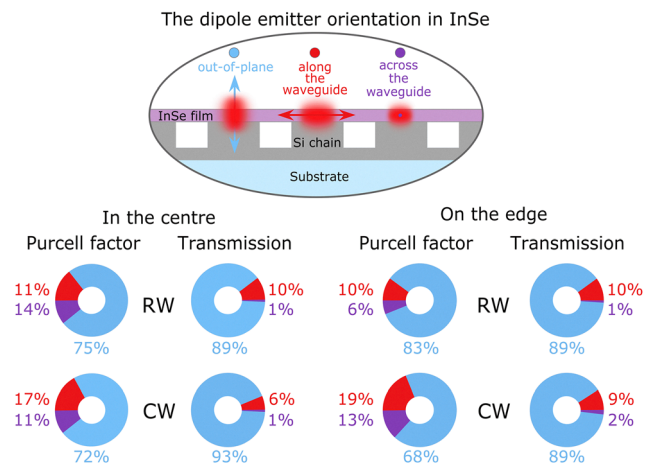


Fig. 6 The influence of dipole emitter orientation in InSe on the Purcell factor and the transmission (amount of power transmitted through the waveguide, normalized to the dipole power) of the RW and the CW.

combined of the all considered dipole configurations. For example, if we integrate all the power collected at the output waveguide port from different emitters located in the InSe film on the resonant waveguide, than 89% of it will be produced by the out-of-plane dipoles, 10% by the dipoles oriented along the waveguide, and only 1% by the dipoles oriented across the waveguide (see the upper row of the pie-charts for transmission). Similar logic is used for the Purcell factor contribution for different dipole configurations. For example, in the case of a dipole placed at the center of the resonant waveguide, the Purcell factor of an out-of-plane orientation is three times greater than for both in-plane orientations. Through analysis of these numerical results one can state that dipoles with out-of-plane orientation provide the highest contribution in all the studied cases. It proves the initial claim that gray excitons with out-of-plane orientation play the dominant role in the observed effects.

7. Discussion

A promising development of this work is the decreasing of absorption losses in the waveguide. It can be achieved through the use of other materials, for example, silicon nitride (Si_3N_4), which is transparent at the visible and NIR wavelengths.⁵¹ However, in this case the design of the waveguide system will likely require modifications, since Si_3N_4 ($n \sim 2.0$) does not have as high refractive index contrast with the SiO_2 substrate ($n \sim 1.5$) as Si ($n \sim 3.6$). In addition, the transition to a single-photon operating mode of an excitonic emitter may be relevant for quantum optics problems. For this purpose, 2D TMDs films can be used, which can compete with more popular single-photon emitters, such as colour centres in diamonds and InAs/GaAs quantum dots.^{40,52}

8. Conclusion

We design and experimentally validate a resonant silicon waveguide with a central part in the form of a chain of

Mie-resonant nanodisks that provides efficient optical coupling with gray excitons in InSe thin film placed on top. The disk parameters are chosen to increase the efficiency of optical coupling between dipole emitters in InSe film and resonant waveguides. Experimental results demonstrate an increase in optical coupling by a factor of 2.5 compared to a conventional rib waveguide. The result obtained in this study may be useful for a variety of integrated photonic applications.

Author contributions

All authors contributed to this article. Numerical calculations and transmission spectra measurements, T. V. A., A. D. G., D. N. G. and A. S. S.; InSe flakes fabrications, M. R. and L. K.; AFM measurements, B. B., micro-Raman measurements, I. E.; Micro-photoluminescence measurements, M. R. and A. G.; writing—original version preparation, T. V. A.; supervising, review and editing, A. A. F.; conceptualization, A. S. S., M. R. and A. A. F.; Methodology A. D. G., A. S. S., M. R. and A. A. F. All authors gave approval for the final version of the manuscript.

Conflicts of interest

The authors have no conflicts of interest.

Data availability

Data supporting the findings of this study are available in the article and its supplementary information (SI). Supplementary information is available. See DOI: <https://doi.org/10.1039/d5tc03144c>.

Acknowledgements

Authors thank the group of Isabelle Staude for help with sample fabrication. The work of M. R. (flakes fabrication and μ -PL measurements) was supported by a grant from the Russian Science Foundation (no. 24-72-00148, <https://rscf.ru/project/24-72-00148/>). The study was conducted under the state assignment of Lomonosov Moscow State University.

References

- 1 I. Kim, R. J. Martins, J. Jang, T. Badloe, S. Khadir, H.-Y. Jung, H. Kim, J. Kim, P. Genevet and J. Rho, *Nat. Nanotechnol.*, 2021, **16**, 508–524.
- 2 M. Estevez, M. Alvarez and L. Lechuga, *Laser Photonics Rev.*, 2011, **6**, 463–487.
- 3 A. Karabchevsky, A. Katiyi, A. S. Ang and A. Hazan, *Nanophotonics*, 2020, **9**, 3733–3753.
- 4 P. Tonndorf, O. Del Pozo-Zamudio, N. Gruhler, J. Kern, R. Schmidt, A. I. Dmitriev, A. P. Bakhtinov, A. I. Tartakovskii, W. Pernice, S. Michaelis de Vasconcellos and R. Bratschitsch, *Nano Lett.*, 2017, **17**, 5446–5451.
- 5 J. A. Dionne, L. A. Sweatlock, M. T. Sheldon, A. P. Alivisatos and H. A. Atwater, *IEEE J. Sel. Top. Quantum Electron.*, 2010, **16**, 295–306.
- 6 J. Wang and Y. Long, *Sci. Bull.*, 2018, **63**, 1267–1310.
- 7 Z. Zhou, B. Yin and J. Michel, *Light: Sci. Appl.*, 2015, **4**, e358–e358.
- 8 K. Lieberman, S. Harush, A. Lewis and R. Kopelman, *Science*, 1990, **247**, 59–61.
- 9 J. Shang, C. Cong, L. Wu, W. Huang and T. Yu, *Small Methods*, 2018, **2**, 1800019.
- 10 S. W. Koch, M. Kira, G. Khitrova and H. M. Gibbs, *Nat. Mater.*, 2006, **5**, 523–531.
- 11 J. Xiao, M. Zhao, Y. Wang and X. Zhang, *Nanophotonics*, 2017, **6**, 1309–1328.
- 12 A. Chernikov, T. C. Berkelbach, H. M. Hill, A. Rigosi, Y. Li, B. Aslan, D. R. Reichman, M. S. Hybertsen and T. F. Heinz, *Phys. Rev. Lett.*, 2014, **113**, 076802.
- 13 F. Xia, H. Wang, D. Xiao, M. Dubey and A. Ramasubramaniam, *Nat. Photonics*, 2014, **8**, 899–907.
- 14 F. Bonaccorso, Z. Sun, T. Hasan and A. C. Ferrari, *Nat. Photonics*, 2010, **4**, 611–622.
- 15 A. K. Geim and I. V. Grigorieva, *Nature*, 2013, **499**, 419–425.
- 16 P. Rivera, J. R. Schaibley, A. M. Jones, J. S. Ross, S. Wu, G. Aivazian, P. Klement, K. Seyler, G. Clark, N. J. Ghimire, J. Yan, D. G. Mandrus, W. Yao and X. Xu, *Nat. Commun.*, 2015, **6**, 6242.
- 17 G. Eda and S. A. Maier, *ACS Nano*, 2013, **7**, 5660–5665.
- 18 A. A. Popkova, I. M. Antropov, G. I. Tselikov, G. A. Ermolaev, I. Ozerov, R. V. Kirtaev, S. M. Novikov, A. B. Evlyukhin, A. V. Arsenin, V. O. Bessonov, V. S. Volkov and A. A. Fedyanin, *Laser Photonics Rev.*, 2022, **16**, 2100604.
- 19 K. F. Mak and J. Shan, *Nat. Photonics*, 2016, **10**, 216–226.
- 20 A. A. Nazarenko, A. M. Chernyak, A. I. Musorin, A. S. Shorokhov, L. Ding, V. Valuckas, M. Nonahal, I. Aharonovich, S. T. Ha, A. I. Kuznetsov and A. A. Fedyanin, *Nanophotonics*, 2024, **13**, 3429–3436.
- 21 F. Peyskens, C. Chakraborty, M. Muneeb, D. Van Thourhout and D. Englund, *Nat. Commun.*, 2019, **10**, 4435.
- 22 G. Wang, C. Robert, M. Glazov, F. Cadiz, E. Courtade, T. Amand, D. Lagarde, T. Taniguchi, K. Watanabe, B. Urbaszek and X. Marie, *Phys. Rev. Lett.*, 2017, **119**, 047401.
- 23 Y. Zhou, G. Scuri, D. S. Wild, A. A. High, A. Dibos, L. A. Jauregui, C. Shu, K. De Greve, K. Pistunova, A. Y. Joe, T. Taniguchi, K. Watanabe, P. Kim, M. D. Lukin and H. Park, *Nat. Nanotechnol.*, 2017, **12**, 856–860.
- 24 X.-X. Zhang, T. Cao, Z. Lu, Y.-C. Lin, F. Zhang, Y. Wang, Z. Li, J. C. Hone, J. A. Robinson, D. Smirnov, S. G. Louie and T. F. Heinz, *Nat. Nanotechnol.*, 2017, **12**, 883–888.
- 25 M. Brotons-Gisbert, R. Proux, R. Picard, D. Andres-Penares, A. Branny, A. Molina-Sanchez, J. F. S. Sanchez-Royo and B. D. Gerardot, *Nat. Commun.*, 2019, **10**, 3913.
- 26 G. W. Mudd, S. A. Svatek, T. Ren, A. Patan, O. Makarovskiy, L. Eaves, P. H. Beton, Z. D. Kovalyuk, G. V. Lashkarev, Z. R. Kudrynskiy and A. I. Dmitriev, *Adv. Mater.*, 2013, **25**, 5714–5718.
- 27 A. Segura, F. Pomer, A. Cantarero, W. Krause and A. Chevy, *Phys. Rev. B: Condens. Matter Mater. Phys.*, 1984, **29**, 5708–5717.

- 28 N. Kuroda and Y. Nishina, *Solid State Commun.*, 1980, **34**, 481–484.
- 29 E. Kress-Rogers, R. Nicholas, J. Portal and A. Chevy, *Solid State Commun.*, 1982, **44**, 379–383.
- 30 N. Leisgang, J. G. Roch, G. Froehlicher, M. Hamer, D. Terry, R. Gorbachev and R. J. Warburton, *AIP Adv.*, 2018, **8**, 105120.
- 31 S. R. Tamalampudi, Y.-Y. Lu, R. K. U, R. Sankar, C.-D. Liao, K. M. B, C.-H. Cheng, F. C. Chou and Y.-T. Chen, *Nano Lett.*, 2014, **14**, 2800–2806.
- 32 S. Lei, L. Ge, S. Najmaei, A. George, R. Koppera, J. Lou, M. Chhowalla, H. Yamaguchi, G. Gupta, R. Vajtai, A. D. Mohite and P. M. Ajayan, *ACS Nano*, 2014, **8**, 1263–1272.
- 33 W. Feng, J.-B. Wu, X. Li, W. Zheng, X. Zhou, K. Xiao, W. Cao, B. Yang, J.-C. Idrobo, L. Basile, W. Tian, P. Tan and P. Hu, *J. Mater. Chem. C*, 2015, **3**, 7022–7028.
- 34 D. N. Gulkin, A. A. Popkova, B. I. Afinogenov, D. A. Shilkin, K. Kuršelis, B. N. Chichkov, V. O. Bessonov and A. A. Fedyanin, *Nanophotonics*, 2021, **10**, 2939–2947.
- 35 D. V. Obydenov, D. A. Shilkin, D. N. Gulkin, E. V. Lyubin, D. M. Zhigunov, V. O. Bessonov and A. A. Fedyanin, *Adv. Opt. Mater.*, 2023, **12**, 2302276.
- 36 A. I. Kuznetsov, A. E. Miroshnichenko, M. L. Brongersma, Y. S. Kivshar and B. Luk'yanchuk, *Science*, 2016, **354**, aag2472.
- 37 A. E. Krasnok, A. E. Miroshnichenko, P. A. Belov and Y. S. Kivshar, *Opt. Express*, 2012, **20**, 20599.
- 38 O. Sergaeva, I. Volkov and R. Savelev, *Nanosyst.: Phys., Chem., Math.*, 2019, **10**, 266–272.
- 39 R. M. Bakker, Y. F. Yu, R. Paniagua-Dominguez, B. Luk'yanchuk and A. I. Kuznetsov, *Nano Lett.*, 2017, **17**, 3458–3464.
- 40 A. D. Gartman, M. K. Kroichuk, A. S. Shorokhov and A. A. Fedyanin, *JETP Lett.*, 2020, **112**, 693–698.
- 41 A. D. Gartman, A. S. Shorokhov and A. A. Fedyanin, *Nanomaterials*, 2023, **13**, 1821.
- 42 C. Song, S. Huang, C. Wang, J. Luo and H. Yan, *J. Appl. Phys.*, 2020, **128**, 060901.
- 43 V. Z. Lyomi, N. D. Drummond and V. I. Fal'ko, *Phys. Rev. B: Condens. Matter Mater. Phys.*, 2014, **89**, 205416.
- 44 B. R. Borodin, I. A. Eliseyev, A. I. Galimov, L. V. Kotova, M. V. Durnev, T. V. Shubina, M. A. Yagovkina and M. V. Rakhlin, *Phys. Rev. Mater.*, 2024, **8**, 014001.
- 45 Y. Y. Wang, Z. H. Ni, Z. X. Shen, H. M. Wang and Y. H. Wu, *Appl. Phys. Lett.*, 2008, **92**, 043121.
- 46 C. Song, F. Fan, N. Xuan, S. Huang, C. Wang, G. Zhang, F. Wang, Q. Xing, Y. Lei, Z. Sun, H. Wu and H. Yan, *Phys. Rev. B*, 2019, **99**, 195414.
- 47 T. Bucher, A. Vaskin, R. Mupparapu, F. J. F. Lichner, A. George, K. E. Chong, S. Fasold, C. Neumann, D.-Y. Choi, F. Eilenberger, F. Setzpfandt, Y. S. Kivshar, T. Pertsch, A. Turchanin and I. Staude, *ACS Photonics*, 2019, **6**, 1002–1009.
- 48 C. Ma, X. Li, P. Huang, X. Liu, J. Yan, Z. Zheng, J. Yao, C. Du, Y. Liu, X. Li, B.-O. Guan and K. Chen, *Adv. Opt. Mater.*, 2025, **13**, 2402015.
- 49 P. Yao, V. Manga Rao and S. Hughes, *Laser Photonics Rev.*, 2010, **4**, 499–516.
- 50 C. Chakraborty, N. Vamivakas and D. Englund, *Nanophotonics*, 2019, **8**, 2017–2032.
- 51 A. Z. Subramanian, P. Neutens, A. Dhakal, R. Jansen, T. Claes, X. Rottenberg, F. Peyskens, S. Selvaraja, P. Helin, B. DuBois, K. Leyssens, S. Severi, P. Deshpande, R. Baets and P. Van Dorpe, *IEEE Photonics J.*, 2013, **5**, 2202809.
- 52 I. Aharonovich, D. Englund and M. Toth, *Nat. Photonics*, 2016, **10**, 631–641.